





Origin of high thermal conductivity in disentangled ultra-high molecular weight polyethylene films: ballistic phonons within enlarged crystals

Taeyong Kim ¹, Stavros X. Drakopoulos ²,
Sara Ronca ² and Austin J. Minnich ^{1,*}

¹*Division of Engineering and Applied Science,
California Institute of Technology, Pasadena, California 91125, USA*

²*Department of Materials, Loughborough University,
Loughborough LE11 3TU, United Kingdom*

(Dated: November 23, 2021)

Abstract

The thermal transport properties of oriented polymers are of fundamental and practical interest. High thermal conductivities ($\gtrsim 50 \text{ Wm}^{-1}\text{K}^{-1}$) have recently been reported in disentangled ultra-high molecular weight polyethylene (UHMWPE) films, considerably exceeding prior reported values for oriented films. However, conflicting explanations have been proposed for the microscopic origin of the high thermal conductivity. Here, we report a characterization of the thermal conductivity and mean free path accumulation function of disentangled UHMWPE films (draw ratio ~ 200) using cryogenic steady-state thermal conductivity measurements and transient grating spectroscopy. We observe a marked dependence of the thermal conductivity on grating period over temperatures from 30 – 300 K. Considering this observation, cryogenic bulk thermal conductivity measurements, and analysis using an anisotropic Debye model, we conclude that longitudinal atomic vibrations with mean free paths around 400 nanometers are the primary heat carriers and that the high thermal conductivity for draw ratio $\gtrsim 150$ arises from the enlargement of extended crystals with drawing. The mean free paths appear to remain limited by the extended crystal dimensions, suggesting that the upper limit of thermal conductivity of disentangled UHMWPE films has not yet been realized.

* aminnich@caltech.edu

I INTRODUCTION

Thermally conductive polymers are of interest for fundamental materials science as well as applications such as thermal management [1–6]. Although the thermal conductivity of unoriented polymers is generally less than $1 \text{ Wm}^{-1}\text{K}^{-1}$ [2], early works reported orders of magnitude increase in uniaxial thermal conductivity of oriented samples, including polyethylene (PE) [7, 8], polyacetylene [9], and polypropylene [10, 11]. In particular, the reported thermal conductivity of oriented polyethylene ranged from $\sim 14 \text{ Wm}^{-1}\text{K}^{-1}$ [12] for draw ratio $DR = 25$ up to $\sim 40 \text{ Wm}^{-1}\text{K}^{-1}$ for solution processed PE with a DR of 350 [13]. The enhancement was attributed to various mechanisms including increased chain alignment along the drawing direction [7, 14], phonon focusing in the elastically anisotropic crystalline phase [15, 16], and increased crystallinity [12, 17]. Recently, thermal conductivity values around $20 - 30 \text{ Wm}^{-1}\text{K}^{-1}$ and $\gtrsim 60 \text{ Wm}^{-1}\text{K}^{-1}$ have been reported in PE microfibers [14, 18] and nanofibers [19, 20], respectively. In macroscopic samples, the introduction of disentangled ultra-high molecular weight polyethylene (UHMWPE) films [21, 22] with higher crystallinities and less entangled amorphous regions compared to prior samples has led to reports of high thermal conductivities exceeding $60 \text{ Wm}^{-1}\text{K}^{-1}$ [23, 24]. Several recent studies have also reported high thermal conductivity up to $20 - 30 \text{ Wm}^{-1}\text{K}^{-1}$ in a diverse set of polymers besides PE, including polybenzobisoxazole [18], polyethylene oxide [25], and amorphous polythiophene [26].

Knowledge of the structural changes that occur upon drawing from nascent PE aid in identifying the origin of the high thermal conductivity values, and extensive studies have characterized the atomic and nanoscale structure of PE films at different DR. The nascent structure consists of spherulites [27] which are in turn composed of unoriented stacked lamella in which folded chains are bridged by intra- and inter-lamella tie molecules [28]. The initial crystalline fraction is on the order of $\sim 60 - 70\%$, as measured using nuclear magnetic resonance (NMR) [29] or heat capacity measurements [30], and from SAXS the crystalline domains have long periods $\sim 10 - 30 \text{ nm}$ [31–33] with the corresponding size of the crystalline domain inside the unit being around 90% of the long period [34]. On drawing, Peterlin proposed a sequence of processes occur in which stacked lamella transition to micro-fibrils and eventually to chain-extended crystals [35]. More precisely, on initial drawing, the lamellae begin to align and a crystalline micro-fibril structure bridged by amorphous domains or tie

molecules emerges as the lamellae are fragmented. Subsequently, for $10 \lesssim DR \lesssim 50$ the micro-fibrils aggregate with concurrent tautening of the tie-molecules and marginal changes in the crystallinity. Finally, for $DR > 50$, chain extension leads to an extended crystal phase formed from the aggregated micro-fibrils and tie-molecules. The density of states and dispersion of atomic vibrations in the crystalline phase have been characterized by various inelastic scattering techniques [36–42].

Experimental evidence in support of the above picture has been obtained using various techniques such as transmission electron microscopy (TEM) [43, 44], SAXS [45], wide angle x-ray scattering (WAXS) [45], and NMR [46, 47], among others [41, 48]. For instance, the formation of the micro-fibrils via lamellae fragmentation is consistent with a lack of a clear trend of crystallite size with DR for $DR \lesssim 10$ [45, 49]. The subsequent unfolding and tautening of tie-molecules along with the aggregation of microfibrils is consistent with an initial rapid increase in crystallinity, elastic modulus and orientation factor with DR below DR 20 [50] followed by a marginal increase of only a few percent up to DR as large as 200 [45, 50, 51]. Evidence for the existence of extended crystal was obtained using various complementary methods such as SAXS and WAXS [47, 49, 52], TEM [43, 44], and NMR [46]. These various techniques indicated that the diameter of the extended crystal is $\sim 10 - 20$ nm and of longitudinal dimension around $100 - 250$ nm or greater [47].

Morphological changes under drawing identified from the above structural studies have provided insight into origin of increase in thermal conductivity. Below $DR \sim 50$, the uni-axial thermal conductivity is observed to monotonically increase with DR [11, 53]. Various effective-medium type models have been proposed to interpret this increase in terms of changes in the crystallinity and crystalline orientation [54–56]. Although these models are generally successful in explaining measured thermal conductivity data, the actual transport processes may differ from those assumed by effective medium theory because of the presence of phonons that are ballistic over multiple crystallites. Evidence of such processes has been reported even in partially oriented PE samples with low $DR \sim 7.5$ using transient grating spectroscopy (TG) [57].

For disentangled UHMWPE of $DR \gtrsim 150$, the increase in thermal conductivity is difficult to interpret using the above models because the thermal conductivity is observed to increase on average by factor of ~ 20 % despite a lack of detectable change in crystallinity or chain orientation [11–13, 23, 24]. Conflicting explanations have been proposed to account for these

observations. For instance, Xu et al. used the isotropic helix-coil model to conclude that the thermal conductivity of the amorphous phase (κ_a) must be as high as $16 \text{ Wm}^{-1}\text{K}^{-1}$ to explain the high thermal conductivity for samples with $\text{DR} \sim 60 \text{ Wm}^{-1}\text{K}^{-1}$ [24]. On the other hand, Ronca et al. used the same model to conclude that the high thermal conductivity for $\text{DR} \gtrsim 150$ originates from the enlargement of the extended crystal dimensions [23]. The discrepancy is difficult to resolve by bulk thermal conductivity measurements because the properties of the crystalline and amorphous phases cannot be independently measured. As a result, the physical origin of the high thermal conductivity of disentangled UHMWPE remains unclear.

Here, we report measurements of the thermal conductivity and mean free path accumulation function of disentangled UHMWPE films ($\text{DR} \sim 200$) using cryogenic thermal conductivity measurements and transient grating spectroscopy. The thermal conductivity exhibits a marked grating dependence, indicating the presence of ballistic heat-carrying atomic vibrations over the length scale of a grating period. We interpret the TG and cryogenic thermal conductivity measurements using an anisotropic Debye model that describes heat transport by longitudinal atomic vibrations. The analysis indicates that the heat is nearly entirely carried by this branch, with values of the temperature-independent mean free paths being around 400 nm up to several THz. Comparing these results to those of our prior study of disentangled UHMWPE films of lower DR, we find that the high thermal conductivity for $\text{DR} \gtrsim 150$ can be attributed to the presence of enlarged extended crystals. As the phonon MFPs appear to be limited by the dimensions of the extended crystals, our study suggests that disentangled UHMWPE films with higher thermal conductivity may be realized in samples with larger extended crystals.

II EXPERIMENT

We measured the in-plane thermal conductivity of disentangled UHMWPE films using TG, as schematically illustrated in Fig. 1(A). The TG setup is identical to that described in Ref. [57]. Briefly, a pair of pump pulses (wavelength 515 nm, beam diameter 530 μm , pulse duration ~ 1 ns, pulse energy 13 μJ , repetition rate 200 Hz) is focused onto the sample to impulsively create a spatially sinusoidal temperature rise of period L and wave vector $q = 2\pi/L$. The grating relaxes by heat conduction, and its decay is monitored by

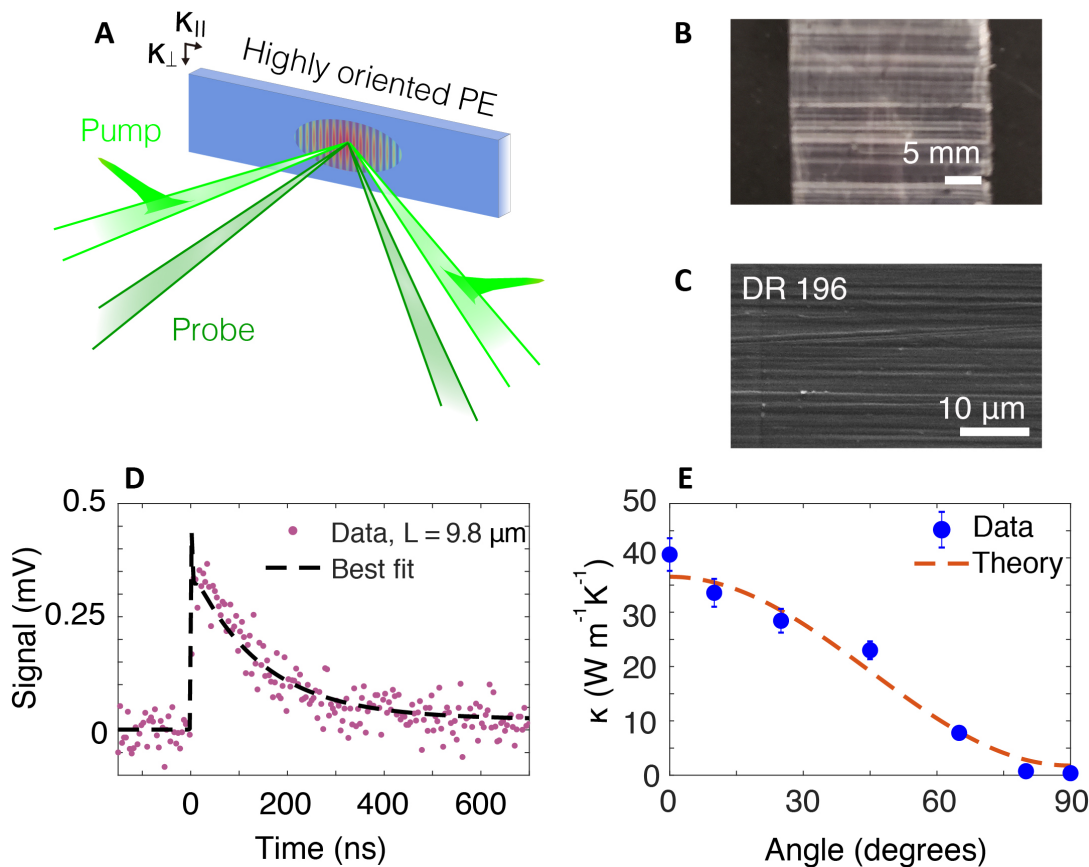


Figure 1. (A) Schematic illustration of transient grating formation and temperature profile in disentangled UHMWPE films. Pump laser pulses impulsively generate a spatial grating on the sample from which probe beams diffract. (B) Optical image of disentangled UHMWPE film (DR = 196). (C) SEM image of the disentangled UHMWPE film. Extended fibers over tens of μm are visible. (D) Representative TG signal versus time for grating period $L = 9.8 \mu m$ at 300 K. The signal is an average of 3×10^4 repetitions at a single location on the sample. The measurement was conducted at multiple locations (see Supplementary Material Sec. 1 for additional data). The thermal diffusivity is obtained as the time constant of the exponential decay. (E) Thermal conductivity versus angle between draw direction and thermal gradient defined by the grating $L = 9.8 \mu m$. The 0° (90°) indicates heat flow direction parallel (perpendicular) to the draw direction. The maximum thermal conductivity is around $40 \text{ W m}^{-1} \text{ K}^{-1}$ along the chain, while the perpendicular value is comparable to that of unoriented PE.

the heterodyne measurement of a diffracted CW signal beam and reference probe beam (wavelength 532 nm, beam diameter 470 μm , CW power 900 μW , chopped at 3.2 % duty cycle to reduce steady heating on the sample). The samples are disentangled UHMWPE films synthesized using the same procedure given in Ref. [21], but with higher draw ratio ($DR = 196$) achieved by rolling ($\times 7$) and stretching ($\times 28$). Figure 1(B) shows an optical image of the film that is of centimeter scale dimension laterally and of thickness around 30 micrometers, as measured using calipers. A scanning electron microscope (SEM) image is given in Fig. 1(C). In both images, highly oriented fibers extending over tens of microns are visible. Since PE is transparent to visible light, Au nanoparticles (diameter: $\sim 2 - 12$ nm [58]; concentration: 1 wt%) were added as an optical absorber. The concentration of the Au was selected to minimize the effect of the filler on the thermal conductivity while enabling the formation of a thermal grating on the sample [57]. Experimental characterization of similar samples using polarized light microscopy, among other methods, indicates that the nanoparticles are oriented in linear chains in the amorphous regions. [58]

A representative TG signal measured at grating period $L = 9.8 \mu\text{m}$ is shown in Fig. 1(D). As described in the Supporting Information of Ref. [57], the signal consists of an initially fast decay (time constant $\lesssim 1$ ns) followed by a slower decay (time constant $\gtrsim 10$ ns). The initial fast decay is attributed to the thermal relaxation of the Au nanoparticles, while the subsequent slower decay corresponds to thermal conduction in the film. Following the procedure in Ref. [57], we fit the signal with a multi-exponential function; the time constant of the slower decay yields the thermal diffusivity of the sample. Because the initial signal from the nanoparticles exhibits a short time constant compared to their thermal signal, the influence of the nanoparticle signal on the fitted thermal diffusivity is negligible. The signal-to-noise ratio (SNR) of the present measurements is generally less than 20, which is about 30% of that reported in Ref. [57] for $DR = 7.5$ samples. This decrease is because the highly oriented samples scatter visible light intensely owing to the increased inhomogeneity over length scales comparable to the optical wavelength, as evidenced by AFM images perpendicular to the fiber alignment direction (see Supplementary Material Sec. 4). Nevertheless, TG is able to measure the thermal signal with adequate SNR because only the diffracted signal due to the spatial refractive index profile at the grating wave vector is measured, and the scattered light intercepted by the detector that does not arise from diffraction can be subtracted from the final signal using a heterodyning procedure [59]. The thermal conductivity

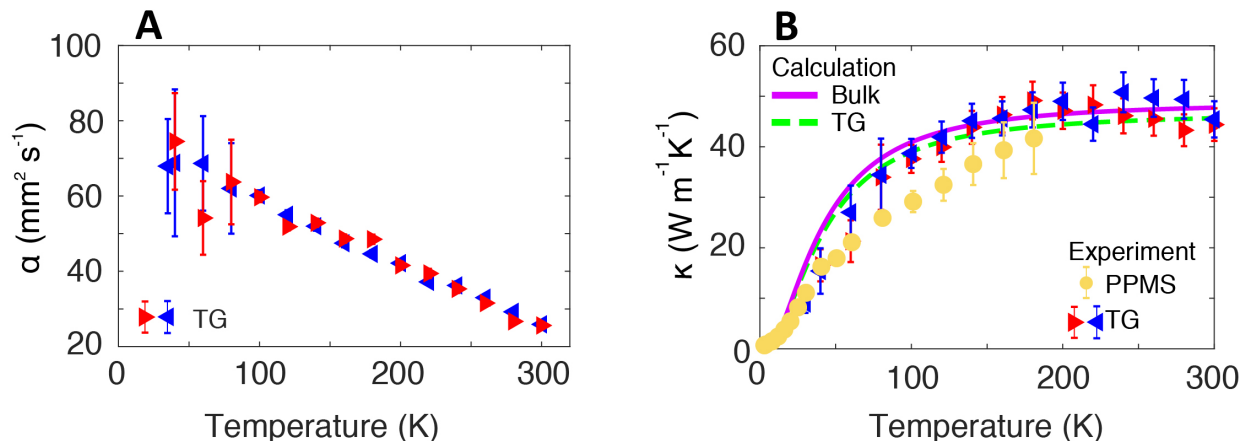


Figure 2. (A) Thermal diffusivity along the chain axis versus temperature for grating period $L = 9.8 \mu\text{m}$. An increase in the thermal diffusivity is observed as temperature decreases. (B) Thermal conductivity along the chain axis versus temperature measured by TG for $L = 9.8 \mu\text{m}$ (blue triangles: cooling, red triangles: heating)) and PPMS (yellow circles). The thermal conductivity is approximately constant from $\sim 300 - 220 \text{ K}$, below which the thermal conductivity decreases. The trend and corresponding values from PPMS and TG with $L = 9.8 \mu\text{m}$ are in reasonable agreement, suggesting that phonon mean free paths are less than $\sim L/2\pi \sim 1.5$ micrometers. Calculated thermal conductivity versus temperature obtained using Eq. 1 (solid purple line: bulk; dashed green line: $L = 9.8 \mu\text{m}$).

was calculated from the measured thermal diffusivity using the heat capacities of linear PE in Ref. [60].

The in-plane thermal conductivity versus angle between the fiber alignment direction and the thermal gradient is shown in Fig. 1(E). The thermal conductivity is $\sim 40 \text{ Wm}^{-1}\text{K}^{-1}$ at 0° (κ_{\parallel} , parallel to grating), and decreases to $0.4 \text{ Wm}^{-1}\text{K}^{-1}$ at 90° (κ_{\perp} , perpendicular to grating). The value along the draw direction is in reasonable agreement with that obtained on a sample without Au nanoparticles using the laser flash method [23]. The value of $\kappa_{\perp} \sim 0.4 \text{ Wm}^{-1}\text{K}^{-1}$ is close to that of unoriented PE, which is attributed to the heat conduction by interchain van der Waals interactions [61]. The angle-dependent thermal conductivity was fitted by a geometric model [62] with the thermal conductivity along the two principal directions as input. Good agreement between the model and the data is observed.

The thermal transport properties can be further examined by measuring the temperature dependence of the thermal diffusivity and conductivity. The bulk thermal diffusivity along the chain direction versus temperature obtained from TG with $L = 9.8$ micrometers between 30 – 300 K is shown in Fig. 2(A). The diffusivity exhibits a linearly increasing trend with decreasing temperature, a qualitatively similar trend as that reported in microscale crystalline fibers [14]. The corresponding κ_{\parallel} versus temperature is shown in Fig. 2(B). Within the uncertainty of the measurement, the thermal conductivity remains constant from room temperature to ~ 220 K, below which the thermal conductivity decreases.

The macroscopic dimensions of the present samples permits additional characterization of the thermal conductivity down to ~ 3 K using a Physical Property Measurement System (PPMS) (See Supplementary Material Sec. 3 for further details). The results are shown in Fig. 2(B). The measured values and the trend of the bulk thermal conductivity are consistent with that obtained from TG. The cryogenic thermal conductivity values on a logarithmic scale are given in Fig. 3. The values exhibit two distinct temperature dependencies with a transition at around 10 K.

The temperature dependence of the thermal diffusivity and conductivity provides insight into the origin of the high thermal conductivity in the present samples. First, the thermal diffusivity is observed to depend on temperature, ruling out a constant relaxation time for all phonon polarizations as suggested in Ref. [20]. Second, the measured trend of thermal conductivity versus temperature is consistent with structural scattering being the dominant scattering mechanism. Above 10 K, the trend is generally consistent with those of previously reported data on PE films of various DR as shown in Fig. 3, although the thermal conductivity of the present sample is consistently higher. Below 10 K, a weaker trend with temperature is observed compared those exhibited by other samples in the same temperature range. This difference may be due to the disentangled nature of the present sample compared to prior solution-cast films and will be the topic of future study. Third, within the uncertainty of the measurements, the measured bulk thermal conductivity is in reasonable agreement with the TG data for $L = 9.8 \mu m$, indicating phonon mean free paths are shorter than $\sim 9.8/2\pi \sim 1.5$ micrometers [65].

Despite these constraints from the temperature-dependent bulk thermal transport properties, the microscopic properties of the heat-carrying atomic vibrations remain underdetermined. To gain further insight, we exploited the ability of TG to systematically vary the

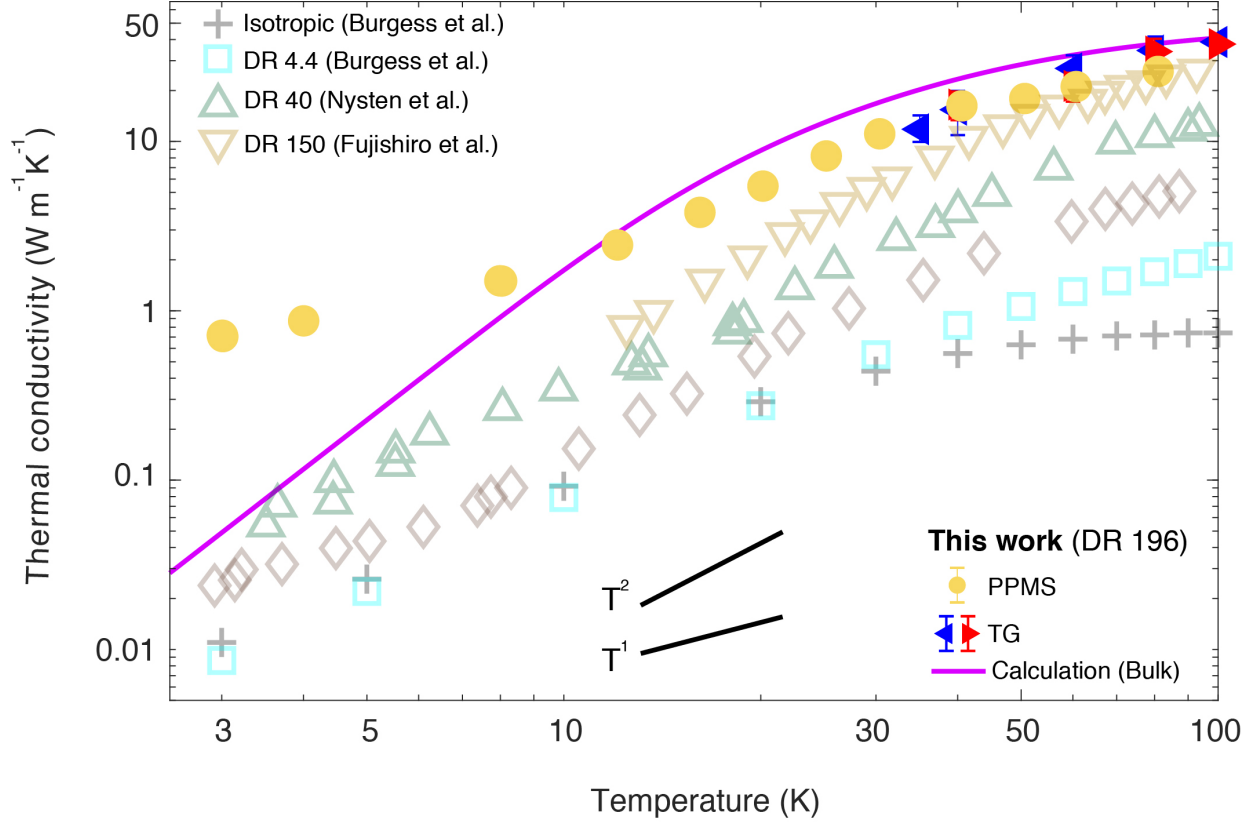


Figure 3. Cryogenic bulk thermal conductivity versus temperatures below 100 K from TG (filled colored triangles), PPMS (yellow circles) and calculated (purple solid line). Representative literature data of thermal conductivity versus temperature for semi-crystalline PE with various DRs are also plotted as open symbols (extruded thin film, DR 4.4, Ref. [8]; solution-cast thin film, DR 40, Ref. [63]; solution-cast macroscopic fiber, DR 150, in Ref. [64]). As temperature decreases, the trend of measured thermal conductivity exhibits a transition from $\sim T^2$ to $\sim T$ near 10 K.

induced thermal gradient over micrometer length scales by tuning the grating period. If heat-carrying phonons propagate ballistically over the grating period, the thermal decay is slower than that predicted from the bulk thermal conductivity [59, 65]. We have previously used this approach to identify ballistic phonons over nanocrystalline domains in disentangled UHMWPE samples of lower DR [57].

We apply this approach to the present samples, measuring the thermal conductivity along the chain axis versus grating period at temperatures of 300 K, 220 K, 100 K, and 35 K. The measured TG signal for a grating period of $L = 1.5 \mu\text{m}$ is shown in the inset of

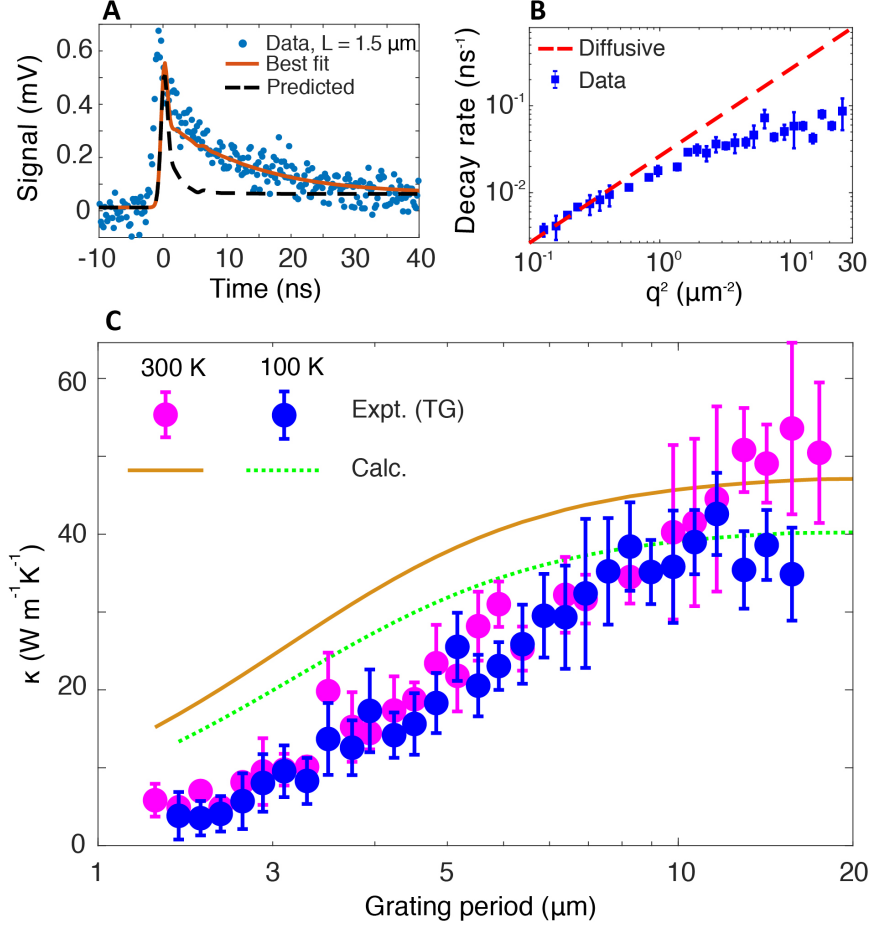


Figure 4. (A) Measured TG signal versus time (symbols) for grating period $L = 1.5 \mu\text{m}$, corresponding to $q^2 \sim 17.5 \mu\text{m}^{-2}$, along with the best fit (solid red line) and predicted decay estimated using the thermal conductivity obtained for $L = 9.8 \mu\text{m}$ (dashed black line). The signal is an average of 5×10^4 shots measured at a single location. The signal clearly decays slower than predicted based on the thermal conductivity measured at larger grating period, indicating a departure from diffusive thermal transport. (B) TG signal decay rate versus q^2 . The measured decay rates for $q^2 \gtrsim 0.3 \mu\text{m}^{-2}$ deviate from that predicted from the thermal conductivity measured at $L = 9.8$ micrometers. (C) Experimental thermal conductivity versus grating period at selected temperatures from experiments (magenta symbols: 300 K; blue symbols: 100 K) along with the calculation (orange solid line: 300 K; green dotted line: 100 K). The thermal conductivity exhibits a marked dependence on grating period and is nearly independent of temperature. Error bars indicate 95% confidence intervals obtained using the procedure given in Ref. [57].

Fig 4(A). The decay is clearly slower than expected based on the bulk thermal conductivity value, indicating the presence of ballistic phonons on the length scale of the grating period. Measurements of the decay rate versus q^2 for all the grating periods at 300 K are given in Fig. 4(B). The measured decay rate is close to that predicted by the bulk thermal conductivity at $q^2 \leq 0.3 \mu\text{m}^{-2}$, above which the decay rate is slower by up to a factor of 5 at the smallest grating period.

The corresponding thermal conductivity versus grating period at 300 K and 100 K is shown in Fig. 4(C). The thermal conductivity exhibits a marked dependence on grating period up to $\sim 10 \mu\text{m}$, a value comparable to that observed in other covalent crystals with higher thermal conductivity such as silicon [59, 66]. Compared to PE samples of lower DR ~ 7.5 [57], the observed trend is significantly more pronounced, indicating the presence of heat-carrying phonons with longer MFPs in the present samples. The observed grating dependence lacks a clear temperature dependence for the temperatures considered here (see Supplementary Material Sec. 3 for additional data). This finding indicates the dominance of the structural scattering, consistent with the trend of the bulk thermal conductivity versus temperature in Fig 2(B).

III LOW ENERGY DEBYE MODEL

We now construct a model to interpret the measurements in Figs 2(B), 3, and 4. We begin by noting that Fig. 4 indicates that phonons with MFPs on the order of hundreds of nanometers carry the majority of the heat. Phonons with such long MFPs are likely from the LA branch owing to its high group velocity $v_c \sim 16 - 17 \text{ km s}^{-1}$ [38–40, 42, 67]. Therefore, the marked dependence of grating period in Fig. 4 implies that nearly all heat is carried by the LA branch. Further, the grating-period dependent thermal conductivity in Fig. 4(C) does not exhibit a temperature dependence, indicating that the MFPs are independent of temperature. We therefore construct an anisotropic Debye model [68, 69] for the heat conducted by this branch and use the data to constrain the frequency-dependence of the LA branch relaxation time. The marked elastic anisotropy of PE can be accounted for to good approximation by assuming the group velocities all point along the chain axis [15]. Therefore, the thermal conductivity measured in TG (κ_i) can be expressed as

$$\kappa_i = \int_0^{\omega_{ab}} S(x_i) [C_1(\omega)v_c\Lambda(\omega)] d\omega + \int_{\omega_{ab}}^{\omega_c} S(x_i) [C_2(\omega)v_c\Lambda(\omega)] d\omega \quad (1)$$

where $q_i = 2\pi L_i^{-1}$, $x_{i,s} = q_i\Lambda_s(\omega)$, $S(x_{i,s})$ is the anisotropic phonon suppression function for an arbitrary phonon dispersion [70], $C_1(\omega)$ and $C_2(\omega)$ refer to the heat capacity terms in Eq. 11b of Ref. [69].

We now specify the numerical values for this model. The c -axis velocity of the longitudinal polarization is $v_c \sim 17 \text{ km s}^{-1}$ [38–40]. The velocity along a perpendicular crystal axis was reported as $v_{ab} \sim 1.35 \text{ km s}^{-1}$ [38] from inelastic neutron scattering and $\sim 4.5 \text{ km s}^{-1}$ from an ab-initio calculation [71] which may be reflective of the monocrystals present in disentangled UHMWPE [21]. We roughly estimate $v_{ab} \sim 3 \text{ km s}^{-1}$. We consider ω_c to be a characteristic frequency at which the c -axis longitudinal velocity decreases below the Debye velocity and ultimately tends towards zero. Roughly, we estimate $\omega_c \sim 10 \text{ THz}$; the analysis below is not sensitive to this choice. This choice then determines $\omega_{ab} = 1.8 \text{ THz}$. The corresponding maximum wave vector magnitude is $\sim 6 \text{ \AA}^{-1}$.

We now seek to identify the function $\Lambda(\omega)$ that best explains the temperature and grating dependence of the thermal conductivity. To constrain the MFP function, we note that at $\sim 1 \text{ THz}$, the magnitude of the MFP can be estimated using the dominant phonon approximation [72] and the cryogenic thermal conductivity measurements in Fig 3. We use the cryogenic thermal conductivity at around 12 K, the minimum temperature that is still on the T^2 trend of the thermal conductivity. We find $\Lambda \sim \kappa/C_l v_l \sim 340 \text{ nm}$ at $\sim 1 \text{ THz}$, where $\kappa \sim 2.45 \text{ Wm}^{-1}\text{K}^{-1}$ and $C_l \sim 4.2 \times 10^{-4} \text{ Jcm}^{-3}\text{K}^{-1}$ is the computed heat capacity of the longitudinal branch at 12 K.

We now consider various MFP profiles versus frequency that yield the best agreement with the experiments in Figs. 2(B), 3, and 4 by adjusting the MFP profile subject to the above constraint. After extensive comparison, we found that the best fit is obtained using a constant $\Lambda \sim 350 - 400 \text{ nm}$ up to $\sim 4.5 - 6 \text{ THz}$, beyond which the MFP decreases as $\sim \omega^{-4}$, although similar power laws also yield reasonable agreement. (See Supplementary Material Sec. 3 for further details on results using other candidate profiles).

The resulting computed bulk thermal conductivity using this profile is presented in Figs. 2(B) and 3. In Fig. 2(B), the bulk thermal conductivity exhibits qualitative agreement with the measurements, producing the observed magnitude and trend. The calculated ther-

mal conductivity in TG with $L = 9.8 \mu\text{m}$ is close to bulk value, consistent with the good agreement between the TG and PPMS measurements. The grating period dependence of the thermal conductivity is also qualitatively reproduced by the calculation in Fig. 4(C), and Fig. S2 in Supplementary Material Sec. 2, although quantitative discrepancies exist.

The calculated cryogenic thermal conductivity is shown in Fig. 3. Although a similar qualitative trend is observed above ~ 10 K, the agreement is worse below this temperature. This discrepancy could be attributed to heat conduction by other types of atomic vibrations which may make the primary contribution to thermal conductivity below ~ 10 K.

IV DISCUSSION

We now discuss our findings in context with prior studies of thermal conduction in oriented PE films. We first consider the MFP value of ~ 400 nm for frequencies in the THz range. For frequencies around 1 THz, prior values inferred from literature data using the dominant phonon approximation at cryogenic temperatures are ~ 80 nm using $\kappa \sim 0.34 \text{ Wm}^{-1}\text{K}^{-1}$ for DR 40 [63], as estimated using LA specific heat of $\sim 2.8 \times 10^{-4} \text{ Jcm}^{-3}\text{K}^{-1}$ at 10 K using the model described above. This value is comparable to an estimated value of ~ 60 nm for DR 6 at 10 K [16]. At higher frequencies ~ 6 THz, IXS has been used to obtain a MFP of ~ 50 nm for DR 5.5 [42], which is in reasonable agreement with the values inferred from transport studies. The MFPs obtained from TG measurements on a DR 7.5 sample in our previous study ranged from 10 - 200 nm [57]. All of these values are comparable to but distinctly smaller than the present value, expected as the present samples exhibit higher thermal conductivity. The decrease in MFP at frequencies exceeding ~ 7 THz is also consistent with the increase in broadening reported in IXS [42], although this increase occurred at higher frequencies in their data.

An average MFP for all LA phonons of ~ 7 nm was estimated from a study of PE microfibers [18]. This value is considerably smaller than those above; as noted in that work, this value is an underestimate owing to the use of the total heat capacity which is greater than that of the longitudinal polarization only. Finally, an ab-initio study of PE predicted MFPs of up to 200 nm [71]. This prediction thus appears to be an underestimate and is likely due to insufficient grid density to sample the stiff LA branch. This observation implies that the predicted thermal conductivity in that work is also an underestimate of the upper

limit of thermal conductivity in crystalline PE.

Our findings help to explain the origin of high thermal conductivity in disentangled UHMWPE films. Recent studies have provided conflicting explanations for the high thermal conductivity, with Xu et al. [24] attributing it to the high thermal conductivity of the amorphous phase [57] but Ronca et al. [23] attributing it to increased extended crystal dimensions. Our data and analysis are consistent with the latter explanation. Compared to the MFPs of a DR 7.5 sample in our prior study,[57] the present MFPs are clearly larger, as would be expected if the extended crystal dimensions have increased. The MFPs in both samples exhibit a clear maximum in the low THz frequencies and are independent of temperature, suggesting phonon scattering is predominantly due to reflections at crystalline domain boundaries. Further, evidence exists for the presence of extended crystals with length on the order of hundreds of nanometers from NMR and TEM [44, 46, 47], values that are compatible with the MFPs obtained here. We infer that heat conduction in disentangled UHMWPE is primarily due to longitudinal atomic vibrations that are ballistic within the extended crystal phase, scattered primarily by reflections at the boundaries between the crystals. Our results therefore support the hypothesis of Ref. [23] in which the high thermal conductivity compared to the prediction including only crystallinity and anisotropy factors for DR $\gtrsim 180$ (Fig. 7 in Ref. [23]) was attributed to the enlargement of extended crystal dimensions.

Finally, we discuss the implications of our findings for realizing PE films of higher thermal conductivity. Because the MFPs appear to be limited by the size of the extended crystals, our study indicates that the thermal conductivity of PE films has not yet reached its upper limit. The practical challenge is synthesizing disentangled UHMWPE films with larger extended crystal dimensions. Such films would be expected to have higher thermal conductivity of an amount proportional to the increase in crystalline dimension.

V SUMMARY

In summary, we have characterized the thermal conductivity and mean free path accumulation function of disentangled UHMWPE films with draw ratio of nearly 200 at various temperatures. We find that heat in PE films is nearly entirely carried by longitudinal atomic vibrations with MFPs in the sub-micron range and limited by the dimensions of the

extended crystal phase. The high thermal conductivity at $DR \gtrsim 150$ exceeding the expected value considering orientation and crystallinity can be attributed to increased dimensions of the extended crystals. Considering the MFPs appear to remain limited by extended crystal dimensions, our work indicates that the thermal conductivity of disentangled UHMWPE films has not yet reached its upper limit.

ACKNOWLEDGMENTS

The authors thank Bolin Liao and Wenkai Ouyang for assistance with PPMS measurements. This work was supported by the Office of Naval Research under Grant Number N00014-18-1-2101.

-
- [1] Hongyu Chen, Valeriy V. Ginzburg, Jian Yang, Yunfeng Yang, Wei Liu, Yan Huang, Libo Du, and Bin Chen. Thermal conductivity of polymer-based composites: Fundamentals and applications. *Progress in Polymer Science*, 59:41–85, August 2016. ISSN 00796700. doi:10.1016/j.progpolymsci.2016.03.001. URL <https://linkinghub.elsevier.com/retrieve/pii/S0079670016000216>.
- [2] James E. Mark, editor. *Physical Properties of Polymers Handbook*. Springer-Verlag, New York, 2 edition, 2007. ISBN 978-0-387-31235-4. doi:10.1007/978-0-387-69002-5. URL <https://www.springer.com/gp/book/9780387312354>.
- [3] Xiangjie Chen, Yuehong Su, David Reay, and Saffa Riffat. Recent research developments in polymer heat exchangers – a review. *Renewable and Sustainable Energy Reviews*, 60:1367–1386, 2016. ISSN 1364-0321. doi:<https://doi.org/10.1016/j.rser.2016.03.024>. URL <https://www.sciencedirect.com/science/article/pii/S1364032116002598>.
- [4] R. Prasher. Thermal interface materials: Historical perspective, status, and future directions. *Proceedings of the IEEE*, 94(8):1571–1586, 2006. doi:10.1109/JPROC.2006.879796.
- [5] Xingfei Wei, Zhi Wang, Zhiting Tian, and Tengfei Luo. Thermal Transport in Polymers: A Review. *Journal of Heat Transfer*, 143(7), 04 2021. ISSN 0022-1481. doi:10.1115/1.4050557. URL <https://doi.org/10.1115/1.4050557>. 072101.
- [6] Congliang Huang, Xin Qian, and Ronggui Yang. Thermal conductivity of polymers and polymer nanocomposites. *Materials Science and Engineering: R: Reports*, 132:1–

- 22, 2018. ISSN 0927-796X. doi:<https://doi.org/10.1016/j.mser.2018.06.002>. URL <https://www.sciencedirect.com/science/article/pii/S0927796X1830113X>.
- [7] D. Hansen and G. A. Bernier. Thermal conductivity of polyethylene: The effects of crystal size, density and orientation on the thermal conductivity. *Polymer Engineering & Science*, 12(3):204–208, 1972. doi:10.1002/pen.760120308. URL <https://onlinelibrary.wiley.com/doi/abs/10.1002/pen.760120308>.
- [8] S Burgess and D Greig. The low-temperature thermal conductivity of polyethylene. *Journal of Physics C: Solid State Physics*, 8(11):1637–1648, jun 1975. doi:10.1088/0022-3719/8/11/015. URL <https://doi.org/10.1088/0022-3719/8/11/015>.
- [9] L Piraux, M Kinany-Alaoui, J. P Issi, D Begin, and D Billaud. Thermal conductivity of an oriented polyacetylene film. *Solid State Communications*, 70(4):427–429, March 1989. ISSN 0038-1098. doi:10.1016/0038-1098(89)91073-9. URL <http://www.sciencedirect.com/science/article/pii/0038109889910739>.
- [10] C L Choy and D Greig. The low temperature thermal conductivity of isotropic and oriented polymers. *Journal of Physics C: Solid State Physics*, 10(2):169–179, jan 1977. doi:10.1088/0022-3719/10/2/005. URL <https://doi.org/10.1088/0022-3719/10/2/005>.
- [11] C. L. Choy, F. C. Chen, and W. H. Luk. Thermal conductivity of oriented crystalline polymers. *Journal of Polymer Science: Polymer Physics Edition*, 18(6):1187–1207, 1980. doi:10.1002/pol.1980.180180603. URL <https://onlinelibrary.wiley.com/doi/abs/10.1002/pol.1980.180180603>.
- [12] C. L Choy, W. H Luk, and F. C Chen. Thermal conductivity of highly oriented polyethylene. *Polymer*, 19(2):155–162, February 1978. ISSN 0032-3861. doi:10.1016/0032-3861(78)90032-0. URL <http://www.sciencedirect.com/science/article/pii/0032386178900320>.
- [13] C. L. Choy, Y. W. Wong, G. W. Yang, and Tetsuo Kanamoto. Elastic modulus and thermal conductivity of ultradrawn polyethylene. *Journal of Polymer Science Part B: Polymer Physics*, 37(23):3359–3367, 1999. ISSN 1099-0488. doi:10.1002/(SICI)1099-0488(19991201)37:23<3359::AID-POLB11>3.0.CO;2-S. URL <https://onlinelibrary.wiley.com/doi/abs/10.1002/%28SICI%291099-0488%2819991201%2937%3A23%3C3359%3A%3AAID-POLB11%3E3.0.CO%3B2-S>.
- [14] Jing Liu, Zaoli Xu, Zhe Cheng, Shen Xu, and Xinwei Wang. Thermal conductivity of ultrahigh molecular weight polyethylene crystal: Defect effect uncovered by 0 k limit phonon diffusion.

- ACS Applied Materials & Interfaces*, 7(49):27279–27288, 2015. doi:10.1021/acsami.5b08578. URL <https://doi.org/10.1021/acsami.5b08578>. PMID: 26593380.
- [15] M. Pietralla, R. M. Weeger, and D. B. Mergenthaler. The role of phonon focussing and structure scattering in oriented semicrystalline polymers. *Zeitschrift für Physik B Condensed Matter*, 77(2):219–228, Jun 1989. ISSN 1431-584X. doi:10.1007/BF01313666. URL <https://doi.org/10.1007/BF01313666>.
- [16] D. B. Mergenthaler and M. Pietralla. Heat conduction in highly oriented polyethylene. *Zeitschrift für Physik B Condensed Matter*, 94(4):461–468, 1994. doi:10.1007/BF01317408. URL <https://doi.org/10.1007/BF01317408>.
- [17] A. G. Gibson, D. Greig, M. Sahota, I. M. Ward, and C. L. Choy. Thermal conductivity of ultrahigh-modulus polyethylene. *Journal of Polymer Science: Polymer Letters Edition*, 15(4):183–192, 1977. doi:10.1002/pol.1977.130150401. URL <https://onlinelibrary.wiley.com/doi/abs/10.1002/pol.1977.130150401>.
- [18] Xiaojia Wang, Victor Ho, Rachel A. Segalman, and David G. Cahill. Thermal conductivity of high-modulus polymer fibers. *Macromolecules*, 46(12):4937–4943, 2013. doi:10.1021/ma400612y. URL <https://doi.org/10.1021/ma400612y>.
- [19] Sheng Shen, Asegun Henry, Jonathan Tong, Ruiting Zheng, and Gang Chen. Polyethylene nanofibres with very high thermal conductivities. *Nature Nanotechnology*, 5(4):251–255, April 2010. ISSN 1748-3395. doi:10.1038/nnano.2010.27. URL <https://www.nature.com/articles/nnano.2010.27>.
- [20] Ramesh Shrestha, Pengfei Li, Bikramjit Chatterjee, Teng Zheng, Xufei Wu, Zeyu Liu, Tengfei Luo, Sukwon Choi, Kedar Hippalgaonkar, Maarten P. de Boer, and Sheng Shen. Crystalline polymer nanofibers with ultra-high strength and thermal conductivity. *Nature Communications*, 9(1):1–9, April 2018. ISSN 2041-1723. doi:10.1038/s41467-018-03978-3. URL <https://www.nature.com/articles/s41467-018-03978-3>.
- [21] Sanjay Rastogi, Yefeng Yao, Sara Ronca, Johan Bos, and Joris van der Eem. Unprecedented high-modulus high-strength tapes and films of ultrahigh molecular weight polyethylene via solvent-free route. *Macromolecules*, 44(14):5558–5568, 2011. doi:10.1021/ma200667m. URL <https://doi.org/10.1021/ma200667m>.
- [22] Sanjay Rastogi, Dirk R. Lippits, Gerrit W. M. Peters, Robert Graf, Yefeng Yao, and Hans W. Spiess. Heterogeneity in polymer melts from melting of polymer crystals. *Nature Materials*, 4

- (8):635–641, Aug 2005. ISSN 1476-4660. doi:10.1038/nmat1437. URL <https://doi.org/10.1038/nmat1437>.
- [23] Sara Ronca, Tamito Igarashi, Giuseppe Forte, and Sanjay Rastogi. Metallic-like thermal conductivity in a lightweight insulator: Solid-state processed Ultra High Molecular Weight Polyethylene tapes and films. *Polymer*, 123:203–210, August 2017. ISSN 0032-3861. doi:10.1016/j.polymer.2017.07.027. URL <http://www.sciencedirect.com/science/article/pii/S0032386117306869>.
- [24] Yanfei Xu, Daniel Kraemer, Bai Song, Zhang Jiang, Jiawei Zhou, James Loomis, Jianjian Wang, Mingda Li, Hadi Ghasemi, Xiaopeng Huang, Xiaobo Li, and Gang Chen. Nanostructured polymer films with metal-like thermal conductivity. *Nature Communications*, 10(1):1–8, April 2019. ISSN 2041-1723. doi:10.1038/s41467-019-09697-7. URL <https://www.nature.com/articles/s41467-019-09697-7>.
- [25] Chenhao Lu, Sum Wai Chiang, Hongda Du, Jia Li, Lin Gan, Xing Zhang, Xiaodong Chu, Youwei Yao, Baohua Li, and Feiyu Kang. Thermal conductivity of electrospinning chain-aligned polyethylene oxide (peo). *Polymer*, 115:52 – 59, 2017. ISSN 0032-3861. doi:<https://doi.org/10.1016/j.polymer.2017.02.024>. URL <http://www.sciencedirect.com/science/article/pii/S0032386117301477>.
- [26] Virendra Singh, Thomas L. Bougher, Annie Weathers, Ye Cai, Kedong Bi, Michael T. Pettes, Sally A. McMenamin, Wei Lv, Daniel P. Resler, Todd R. Gattuso, David H. Altman, Kenneth H. Sandhage, Li Shi, Asegun Henry, and Baratunde A. Cola. High thermal conductivity of chain-oriented amorphous polythiophene. *Nature Nanotechnology*, 9(5):384–390, 2014. doi:10.1038/nnano.2014.44. URL <https://doi.org/10.1038/nnano.2014.44>.
- [27] C. W. Bunn and T. C. Alcock. The texture of polythene. *Trans. Faraday Soc.*, 41:317–325, 1945. doi:10.1039/TF9454100317. URL <http://dx.doi.org/10.1039/TF9454100317>.
- [28] A Keller. Polymer crystals. *Reports on Progress in Physics*, 31(2):623–704, jul 1968. doi:10.1088/0034-4885/31/2/304. URL <https://doi.org/10.1088/0034-4885/31/2/304>.
- [29] C. W. Wilson III and G. E. Pake. Nuclear magnetic resonance determination of degree of crystallinity in two polymers. *Journal of Polymer Science*, 10(5):503–505, 1953. doi:<https://doi.org/10.1002/pol.1953.120100508>. URL <https://onlinelibrary.wiley.com/doi/abs/10.1002/pol.1953.120100508>.

- [30] A. Peterlin and G. Meinel. Heat content of amorphous regions of drawn linear polyethylene. *Journal of Polymer Science Part B: Polymer Letters*, 3(9):783–787, 1965. doi:<https://doi.org/10.1002/pol.1965.110030919>. URL <https://onlinelibrary.wiley.com/doi/abs/10.1002/pol.1965.110030919>.
- [31] E. W. Fischer and G. F. Schmidt. Long periods in drawn polyethylene. *Angewandte Chemie International Edition in English*, 1(9):488–499, 1962. doi:<https://doi.org/10.1002/anie.196204881>. URL <https://onlinelibrary.wiley.com/doi/abs/10.1002/anie.196204881>.
- [32] K. KOBAYASHI and M. KUROKAWA. Small-angle diffraction of polyethylene. *Nature*, 196 (4854):538–539, Nov 1962. ISSN 1476-4687. doi:10.1038/196538a0. URL <https://doi.org/10.1038/196538a0>.
- [33] G. S. Y. Yeh and P. H. Geil. Selected-area small-angle electron diffraction. *Journal of Materials Science*, 2(5):457–469, Sep 1967. ISSN 1573-4803. doi:10.1007/BF00562952. URL <https://doi.org/10.1007/BF00562952>.
- [34] Phillip H. Geil, Franklin R. Anderson, Bernhard Wunderlich, and Tamio Arakawa. Morphology of polyethylene crystallized from the melt under pressure. *Journal of Polymer Science Part A: General Papers*, 2(8):3707–3720, 1964. doi:<https://doi.org/10.1002/pol.1964.100020829>. URL <https://onlinelibrary.wiley.com/doi/abs/10.1002/pol.1964.100020829>.
- [35] A. Peterlin. Molecular model of drawing polyethylene and polypropylene. *Journal of Materials Science*, 6(6):490–508, Jun 1971. ISSN 1573-4803. doi:10.1007/BF00550305. URL <https://doi.org/10.1007/BF00550305>.
- [36] H. R. Danner, H. Boutin, and G. J. Safford. Low-frequency molecular vibrations in solid hexane by neutron inelastic scattering. *The Journal of Chemical Physics*, 41(11):3649–3650, 1964. doi:10.1063/1.1725784. URL <https://doi.org/10.1063/1.1725784>.
- [37] G. J. Safford and A. W. Naumann. Low frequency motions in polymers as measured by neutron inelastic scattering. In *Fortschritte der Hochpolymeren-Forschung*, pages 1–27, Berlin, Heidelberg, 1967. Springer Berlin Heidelberg. ISBN 978-3-540-34908-2.
- [38] L. Holliday and J. W. White. The stiffness of polymers in relation to their structure:. *Pure and Applied Chemistry*, 26(3-4):545–582, 1971. doi:doi:10.1351/pac197126030545. URL <https://doi.org/10.1351/pac197126030545>.

- [39] L. A. Feldkamp, G. Venkataraman, and J. S. King. *Dispersion Relation for Skeletal Vibrations in Deuterated Polyethylene*. IAEA, International Atomic Energy Agency (IAEA), 1968. URL http://inis.iaea.org/search/search.aspx?orig_q=RN:44068946.
- [40] J.F Twisleton, J.W White, and P.A Reynolds. Dynamical studies of fully oriented deuteropolyethylene by inelastic neutron scattering. *Polymer*, 23(4):578–588, 1982. ISSN 0032-3861. doi:[https://doi.org/10.1016/0032-3861\(82\)90097-0](https://doi.org/10.1016/0032-3861(82)90097-0). URL <https://www.sciencedirect.com/science/article/pii/0032386182900970>.
- [41] D. Heyer, U. Buchenau, and M. Stamm. Determination of elastic shear constants of polyethylene at room temperature by inelastic neutron scattering. *Journal of Polymer Science: Polymer Physics Edition*, 22(8):1515–1527, 1984. doi:<https://doi.org/10.1002/pol.1984.180220814>. URL <https://onlinelibrary.wiley.com/doi/abs/10.1002/pol.1984.180220814>.
- [42] A. Mermet, L. David, M. Lorenzen, and M. Krisch. Inelastic x-ray scattering from stretch-oriented polyethylene. *The Journal of Chemical Physics*, 119(3):1879–1884, 2003. doi:10.1063/1.1579681. URL <https://doi.org/10.1063/1.1579681>.
- [43] Paul Smith, Alain Boudet, and Henri Chanzy. The structure of ultradrawn high molecular weight polyethylene revealed by electron microscopy at 100 and 1500 kV. *Journal of Materials Science Letters*, 4(1):13–18, January 1985. ISSN 0261-8028, 1573-4811. doi:10.1007/BF00719883. URL <http://link.springer.com/10.1007/BF00719883>.
- [44] Jean M. Brady and Edwin L. Thomas. Conversion of single crystal mats to ultrahigh modulus polyethylene: the formation of a continuous crystalline phase. *Polymer*, 30(9):1615 – 1622, 1989. ISSN 0032-3861. doi:[https://doi.org/10.1016/0032-3861\(89\)90320-0](https://doi.org/10.1016/0032-3861(89)90320-0). URL <http://www.sciencedirect.com/science/article/pii/0032386189903200>.
- [45] N. A. J. M. Van Aerle and A. W. M. Braam. A structural study on solid state drawing of solution-crystallized ultra-high molecular weight polyethylene. *Journal of Materials Science*, 23(12):4429–4436, 1988. doi:10.1007/BF00551941. URL <https://doi.org/10.1007/BF00551941>.
- [46] W.-G Hu and K Schmidt-Rohr. Characterization of ultradrawn polyethylene fibers by nmr: crystallinity, domain sizes and a highly mobile second amorphous phase. *Polymer*, 41(8):2979 – 2987, 2000. ISSN 0032-3861. doi:[https://doi.org/10.1016/S0032-3861\(99\)00429-2](https://doi.org/10.1016/S0032-3861(99)00429-2). URL <http://www.sciencedirect.com/science/article/pii/S0032386199004292>.

- [47] V. M. Litvinov, Jianjun Xu, C. Melian, D. E. Demco, M. Möller, and J. Simmelink. Morphology, chain dynamics, and domain sizes in highly drawn gel-spun ultrahigh molecular weight polyethylene fibers at the final stages of drawing by saxs, waxes, and 1h solid-state nmr. *Macromolecules*, 44(23):9254–9266, 2011. doi:10.1021/ma201888f. URL <https://doi.org/10.1021/ma201888f>.
- [48] S. N. Magonov, S. S. Sheiko, R. A. C. Deblieck, and M. Moller. Atomic-force microscopy of gel-drawn ultrahigh-molecular-weight polyethylene. *Macromolecules*, 26(6):1380–1386, 1993. doi:10.1021/ma00058a029. URL <https://doi.org/10.1021/ma00058a029>.
- [49] Y. A. Zubov, S. N. Chvalun, V. I. Selikhova, M. B. Konstantinopolskaya, and N. Ph. Bakeev. The structure of highly oriented high modulus polyethylene. *Polymer Engineering & Science*, 32(17):1316–1324, 1992. doi:10.1002/pen.760321720. URL <https://onlinelibrary.wiley.com/doi/abs/10.1002/pen.760321720>.
- [50] K. Anandakumaran, S. K. Roy, and R. St. John Manley. Drawing-induced changes in the properties of polyethylene fibers prepared by gelation/crystallization. *Macromolecules*, 21(6):1746–1751, 1988. doi:10.1021/ma00184a036. URL <https://doi.org/10.1021/ma00184a036>.
- [51] Richard S. Stein and Forrest H. Norris. The x-ray diffraction, birefringence, and infrared dichroism of stretched polyethylene. *Journal of Polymer Science*, 21(99):381–396, 1956. doi:https://doi.org/10.1002/pol.1956.120219903. URL <https://onlinelibrary.wiley.com/doi/abs/10.1002/pol.1956.120219903>.
- [52] Yujing Tang, Zhiyong Jiang, Yongfeng Men, Lijia An, Hans-Friedrich Enderle, Dieter Lilge, Stephan V. Roth, Rainer Gehrke, and Jens Rieger. Uniaxial deformation of overstretched polyethylene: In-situ synchrotron small angle x-ray scattering study. *Polymer*, 48(17):5125 – 5132, 2007. ISSN 0032-3861. doi:https://doi.org/10.1016/j.polymer.2007.06.056. URL <http://www.sciencedirect.com/science/article/pii/S0032386107006313>.
- [53] C. L. Choy, Y. Fei, and T. G. Xi. Thermal conductivity of gel-spun polyethylene fibers. *Journal of Polymer Science Part B: Polymer Physics*, 31(3):365–370, 1993. doi:10.1002/polb.1993.090310315. URL <https://onlinelibrary.wiley.com/doi/abs/10.1002/polb.1993.090310315>.
- [54] Jürgen Hennig. Anisotropy and structure in uniaxially stretched amorphous high polymers. *Journal of Polymer Science Part C: Polymer Symposia*, 16(5):2751–2761, 1967. doi:10.1002/polc.5070160528. URL <https://onlinelibrary.wiley.com/doi/abs/10.1002/polc.5070160528>.





- [polc.5070160528](#).
- [55] C.L. Choy and K. Young. Thermal conductivity of semicrystalline polymers — a model. *Polymer*, 18(8):769–776, 1977. ISSN 0032-3861. doi:[https://doi.org/10.1016/0032-3861\(77\)90179-3](https://doi.org/10.1016/0032-3861(77)90179-3). URL <https://www.sciencedirect.com/science/article/pii/0032386177901793>.
- [56] Motowo Takayanagi, Shinsaku Uemura, and Shunsuke Minami. Application of equivalent model method to dynamic rheo-optical properties of crystalline polymer. *Journal of Polymer Science Part C: Polymer Symposia*, 5(1):113–122, 1964. doi:10.1002/polc.5070050111. URL <https://onlinelibrary.wiley.com/doi/abs/10.1002/polc.5070050111>.
- [57] Andrew B. Robbins, Stavros X. Drakopoulos, Ignacio Martin-Fabiani, Sara Ronca, and Austin J. Minnich. Ballistic thermal phonons traversing nanocrystalline domains in oriented polyethylene. *Proceedings of the National Academy of Sciences*, 116(35):17163–17168, August 2019. ISSN 0027-8424, 1091-6490. doi:10.1073/pnas.1905492116. URL <https://www.pnas.org/content/116/35/17163>.
- [58] Stavros X. Drakopoulos, Oreste Tarallo, Linlin Guan, Ignacio Martin-Fabiani, and Sara Ronca. Nanocomposites of au/disentangled uhmwpe: A combined optical and structural study. *Molecules*, 25(14), 2020. ISSN 1420-3049. doi:10.3390/molecules25143225. URL <https://www.mdpi.com/1420-3049/25/14/3225>.
- [59] Jeremy A. Johnson, A. A. Maznev, John Cuffe, Jeffrey K. Eliason, Austin J. Minnich, Timothy Kehoe, Clivia M. Sotomayor Torres, Gang Chen, and Keith A. Nelson. Direct measurement of room-temperature nondiffusive thermal transport over micron distances in a silicon membrane. *Phys. Rev. Lett.*, 110:025901, Jan 2013. doi:10.1103/PhysRevLett.110.025901. URL <https://link.aps.org/doi/10.1103/PhysRevLett.110.025901>.
- [60] SS Chang. Heat capacities of polyethylene from 2 to 360 k. ii. two high density linear polyethylene samples and thermodynamic properties of crystalline linear polyethylene. *J. Res. NBS A Phys. Chem*, 3, 1974.
- [61] C.L. Choy. Thermal conductivity of polymers. *Polymer*, 18(10):984 – 1004, 1977. ISSN 0032-3861. doi:[https://doi.org/10.1016/0032-3861\(77\)90002-7](https://doi.org/10.1016/0032-3861(77)90002-7). URL <http://www.sciencedirect.com/science/article/pii/0032386177900027>.
- [62] E. Zolotoyabko. *Basic Concepts of Crystallography*. Wiley, 2011. ISBN 9783527330096. URL <https://books.google.com/books?id=eNdJYgEACAAJ>. in page 195.

- [63] B. Nysten, P. Gonry, and J.-P. Issi. Intra- and interchain thermal conduction in polymers. *Synthetic Metals*, 69(1):67–68, 1995. ISSN 0379-6779. doi: [https://doi.org/10.1016/0379-6779\(94\)02366-7](https://doi.org/10.1016/0379-6779(94)02366-7). URL <https://www.sciencedirect.com/science/article/pii/0379677994023667>. Proceedings of the International Conference on Science and Technology of Synthetic Metals.
- [64] Hiroyuki Fujishiro, Manabu Ikebe, Toshihiro Kashima, and Atsuhiko Yamanaka. Drawing effect on thermal properties of high-strength polyethylene fibers. *Japanese Journal of Applied Physics*, 37(Part 1, No. 4A):1994–1995, apr 1998. doi:10.1143/jjap.37.1994. URL <https://doi.org/10.1143/jjap.37.1994>.
- [65] A. J. Minnich. Determining phonon mean free paths from observations of quasiballistic thermal transport. *Phys. Rev. Lett.*, 109:205901, Nov 2012. doi:10.1103/PhysRevLett.109.205901. URL <https://link.aps.org/doi/10.1103/PhysRevLett.109.205901>.
- [66] Navaneetha K. Ravichandran, Hang Zhang, and Austin J. Minnich. Spectrally resolved specular reflections of thermal phonons from atomically rough surfaces. *Phys. Rev. X*, 8:041004, Oct 2018. doi:10.1103/PhysRevX.8.041004. URL <https://link.aps.org/doi/10.1103/PhysRevX.8.041004>.
- [67] M. Pietralla. High thermal conductivity of polymers: Possibility or dream? *Journal of Computer-Aided Materials Design*, 3(1):273–280, Aug 1996. ISSN 1573-4900. doi:10.1007/BF01185664. URL <https://doi.org/10.1007/BF01185664>.
- [68] J.C. Bowman and J.A. Krumhansl. The low-temperature specific heat of graphite. *Journal of Physics and Chemistry of Solids*, 6(4):367–379, 1958. ISSN 0022-3697. doi: [https://doi.org/10.1016/0022-3697\(58\)90055-6](https://doi.org/10.1016/0022-3697(58)90055-6). URL <https://www.sciencedirect.com/science/article/pii/0022369758900556>.
- [69] Z. Chen, Z. Wei, Y. Chen, and C. Dames. Anisotropic debye model for the thermal boundary conductance. *Phys. Rev. B*, 87:125426, Mar 2013. doi:10.1103/PhysRevB.87.125426. URL <https://link.aps.org/doi/10.1103/PhysRevB.87.125426>.
- [70] A. J. Minnich. Phonon heat conduction in layered anisotropic crystals. *Phys. Rev. B*, 91:085206, Feb 2015. doi:10.1103/PhysRevB.91.085206. URL <https://link.aps.org/doi/10.1103/PhysRevB.91.085206>.
- [71] Nina Shulumba, Olle Hellman, and Austin J. Minnich. Lattice thermal conductivity of polyethylene molecular crystals from first-principles including nuclear quantum effects. *Phys.*

Rev. Lett., 119:185901, Oct 2017. doi:10.1103/PhysRevLett.119.185901. URL <https://link.aps.org/doi/10.1103/PhysRevLett.119.185901>.

- [72] R. C. Zeller and R. O. Pohl. Thermal conductivity and specific heat of noncrystalline solids. *Phys. Rev. B*, 4:2029–2041, Sep 1971. doi:10.1103/PhysRevB.4.2029. URL <https://link.aps.org/doi/10.1103/PhysRevB.4.2029>.

**Supporting information: Origin of high thermal conductivity in disentangled
ultra-high molecular weight polyethylene films: ballistic phonons within
enlarged crystals**

Taeyong Kim ¹, Stavros X. Drakopoulos ², Sara Ronca ² and Austin J. Minnich ^{1,*}

*¹Division of Engineering and Applied Science,
California Institute of Technology, Pasadena, California 91125, USA*

*²Department of Materials, Loughborough University,
Loughborough LE11 3TU, United Kingdom*

(Dated: November 23, 2021)

* aminnich@caltech.edu

SI. ADDITIONAL TRANSIENT GRATING DATA

Additional TG data for various grating periods and temperatures are presented below.

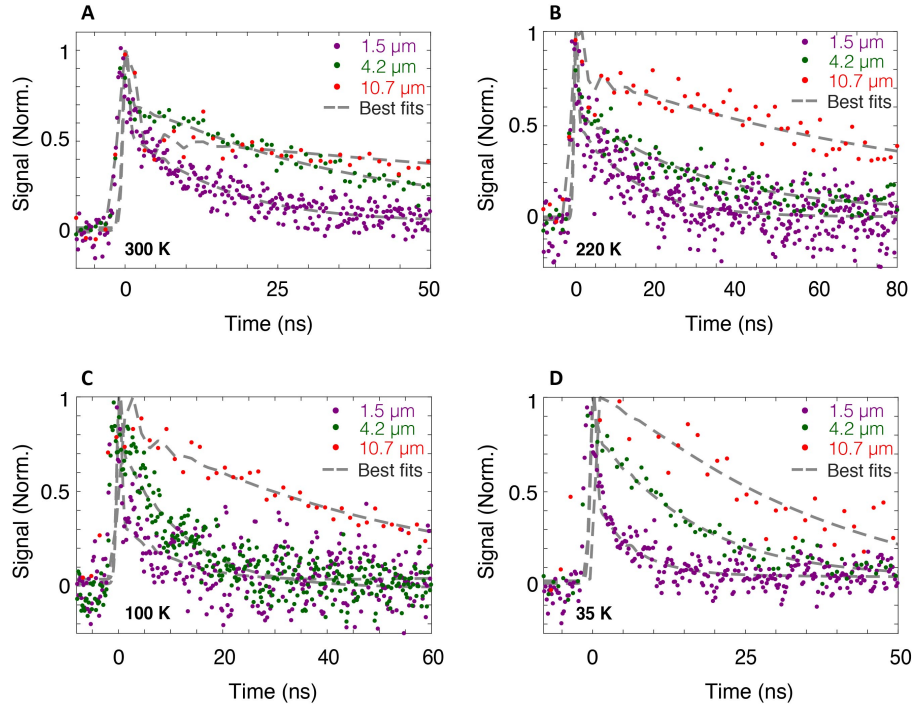


Figure SI. Additional TG measurements and corresponding best fits for grating periods of 1.5 μm , 4.2 μm , and 10.7 μm at (A) 300 K (B) 220 K (C) 100 K (D) 35 K.

SII. THERMAL CONDUCTIVITY VERSUS GRATING PERIOD

Additional measurements of thermal conductivity versus grating period at 220 K and 35 K are shown in Fig. SII along with the model predictions. The model captures the general trend although quantitative discrepancies remain.

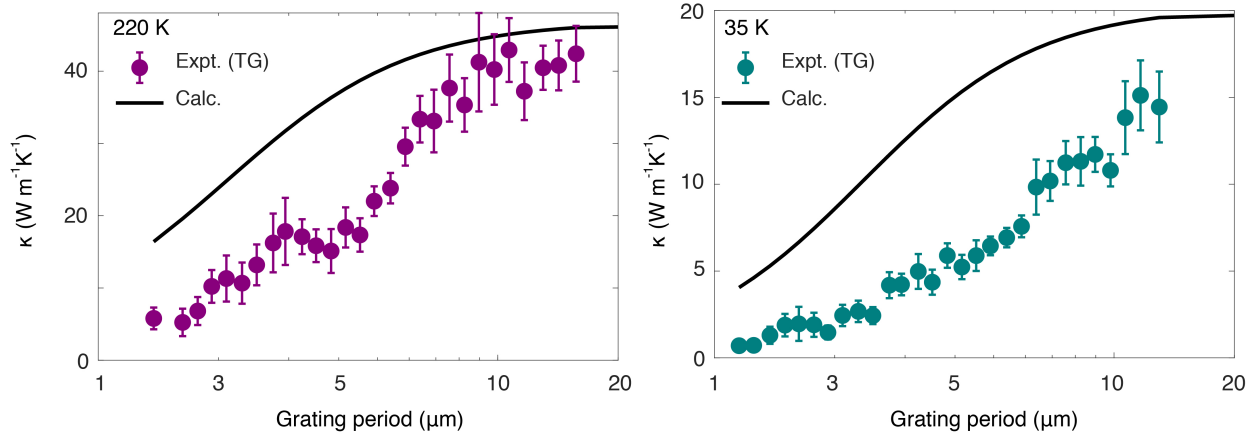


Figure SII. Measured thermal conductivity versus grating period along with the fit based on an anisotropic Debye model at (A) 220 K and (B) 35 K.

SIII. COMPUTED THERMAL CONDUCTIVITY VERSUS GRATING PERIOD VERSUS TEMPERATURE USING OTHER CANDIDATE PROFILES

This section presents calculated thermal conductivity using alternate trends for the LA branch relaxation time versus frequency. The first trend is a constant MFP of 400 nm that transitions to ω^{-1} at 7 THz, shown in Fig. SIII; the second is a constant MFP of 400 nm that transitions to ω^{-2} at 7 THz, shown in Fig. SIV. Power laws with larger exponents generally exhibit improved agreement of thermal conductivity versus grating period.

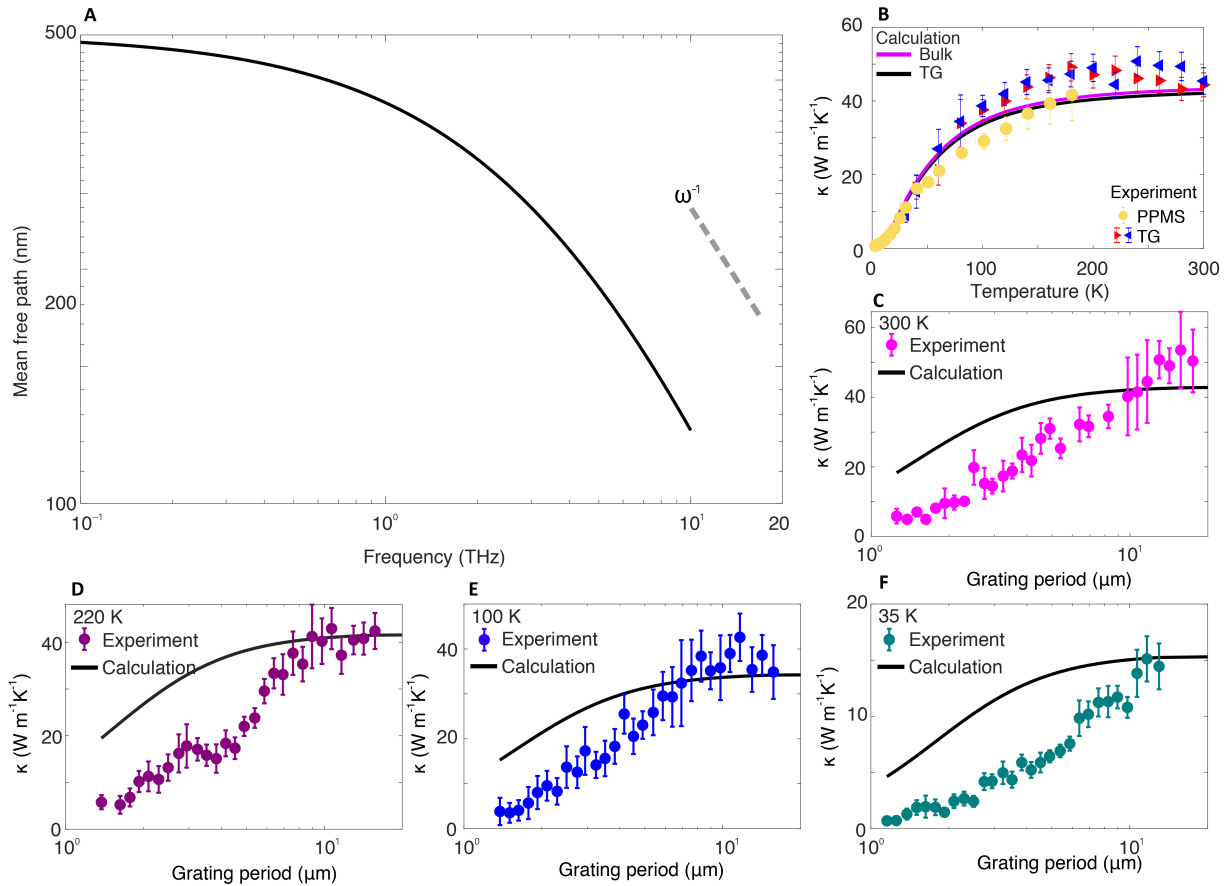


Figure SIII. (A) Candidate MFP profile versus frequency (Constant value (400nm) to ω^{-1} , transition frequency ~ 7 THz). (B) Calculated bulk thermal conductivity versus temperature using the profile in (A). Calculated thermal conductivity versus grating period at (C) 300 K, (D) 220 K, (E) 100 K, and (F) 35 K using the profile in (A).

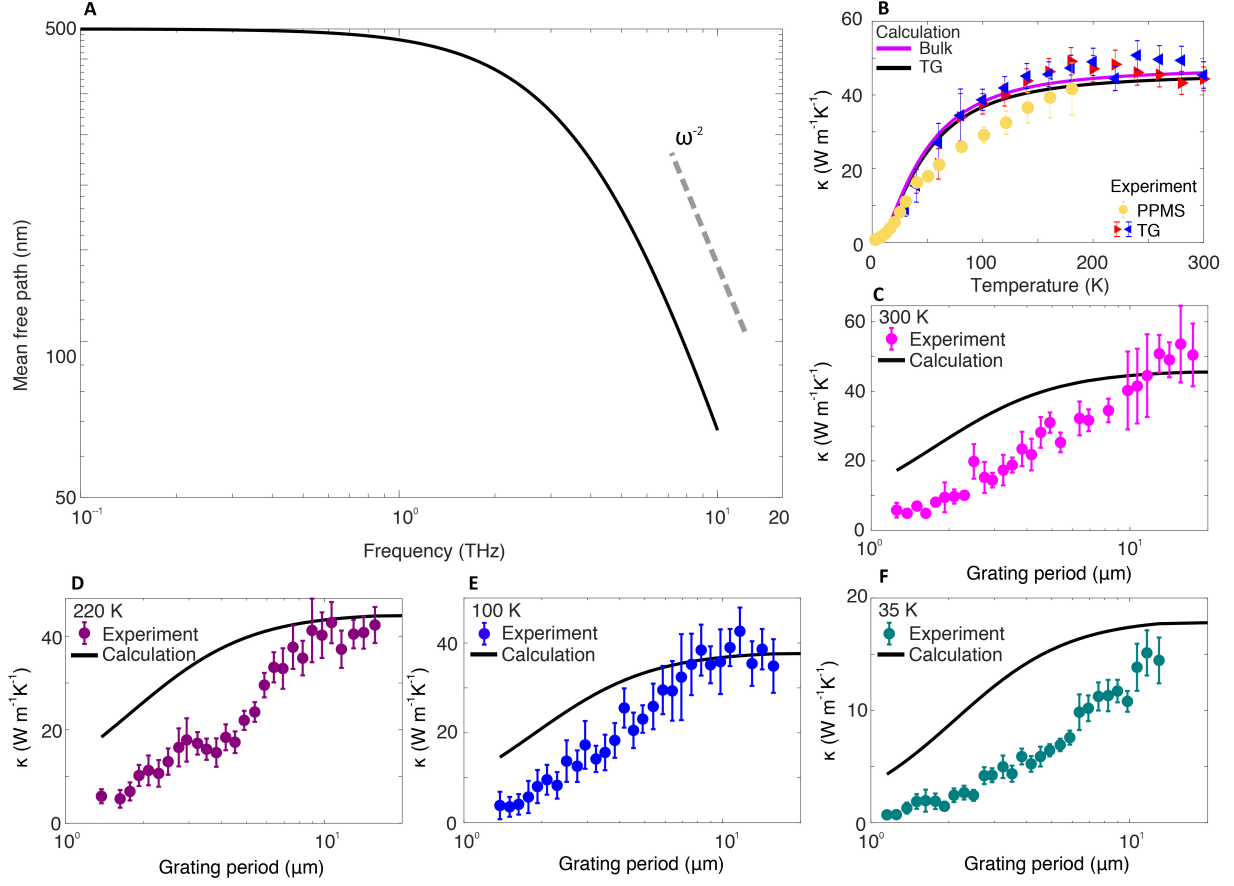


Figure SIV. (A) Candidate MFP profile versus frequency (Constant value (400nm) to ω^{-2} , transition frequency ~ 7 THz). (B) Calculated bulk thermal conductivity versus temperature using the profile in (A). Calculated thermal conductivity versus grating period at (C) 300 K, (D) 220 K, (E) 100 K, and (F) 35 K using the profile in (A).

SIV. DETAILS OF THE PHYSICAL PROPERTY MEASUREMENT SYSTEM MEASUREMENTS

We performed bulk thermal conductivity measurements at cryogenic temperatures using a commercial 7 T Dynacool Physical Property Measurement System (PPMS, Quantum Design). Samples of 196 DR (thickness: $30\ \mu\text{m}$, as measured using the calipers and cross-sectional view from scanning electron microscopy; lateral width: 1.62 mm; heat conduction length excluding electrical contact: 5.6 mm) were mounted in a four-point electrical contact geometry. Silver conducting epoxy was applied between the sample and the four copper wires and cured for 7 hours at $\sim 400\ \text{K}$ on a hot plate. Following Refs. [1, 2], we additionally applied a cryogenic varnish on top of the epoxy (GE7031, Lakeshore) to ensure both the physical and the thermal contact between the wires and the sample; the varnish was cured at room temperature for 24 hours and then transferred onto a thermal transport platform.

PPMS measurements were conducted at temperatures ranging from $\sim 3 - 200\ \text{K}$. At each temperature, we adjusted the electrical heater power to minimize the temperature rise and temperature fluctuations during thermal equilibration. Table SI, shows the base temperature and peak temperature along with the electrical power. The temperature rise was constrained to be from 1.3 - 3.5% of the base temperature. To account for radiative heat loss, we used an emissivity of 0.1 as given in Ref. [3].

Table SI. Measured sample temperature and electrical power used in PPMS.

Base sample temperature (K)	Heater power (μW)	Peak temperature (K)
3	0.3	3.0
3	0.5	3.1
4	0.6	4.1
8	4	8.3
12	8	12.4
16	20	16.7
20	30	20.7
25	50	25.8
30	120	31.5
41	240	42.0
50	320	52.4
61	400	62.5
81	700	83.5
101	950	104.1
121	1.2×10^3	124.4
141	1.05×10^3	143.2
161	1.45×10^3	163.9
181	1.48×10^3	183.5

SV. STEADY HEATING AT 30 K

We estimate the steady heating due to the pump and probe pulses at 30 K. At higher temperatures, the thermal conductivity of the sample is high enough that the steady temperature rise relative to the base temperature can be neglected. Given the laser beam diameter $d = 550 \mu\text{m}$, and heat conduction length $l = 10 \text{ mm}$ (see Fig. 1B), the steady temperature rise considering 1D heat conduction along the drawing direction can be expressed as

$$\Delta T = \frac{l}{A} \frac{P_{abs,total}}{\kappa} \quad (\text{S1})$$

where $A = dt \simeq 550 \mu\text{m} \times 30 \mu\text{m} = 1.7 \times 10^{-8} \text{ m}^2$ is the cross-sectional area, $P_{abs,total} = \alpha P_{total}$ is the absorbed average power with incident optical power P_{total} , and κ is the thermal conductivity at 30 K ($\sim 10 \text{ Wm}^{-1}\text{K}^{-1}$). P_{total} was calculated to be $\sim 1.75 \text{ mW}$, using $P_{total} = (1/2)(E_{pump} \times f_{rep} + P_{probe})$ where E_{pump} is incident pump energy ($\sim 13 \mu\text{J}$), f_{rep} is laser repetition rate (200 Hz), and P_{probe} is the steady incident probe power ($\approx 900 \mu\text{W}$). The factor of 1/2 accounts for heat conduction in both directions from the center of the film to the edges. Since experimentally determining α of the sample is challenging due to intense optical scattering of the sample, α was roughly estimated as $\sim 5\%$. The resulting steady temperature rise is estimated to be $\Delta T \sim 10 \text{ mm} / (1.7 \times 10^{-8} \text{ m}^2) \times (1.75 \text{ mW} \times 0.05 / 10 \text{ Wm}^{-1}\text{K}^{-1}) \sim 5.3 \text{ K}$. Therefore, we take the temperature of the sample for a base temperature of 30 K to be $\sim 35 \text{ K}$.

SVI. SURFACE CHARACTERIZATION USING ATOMIC FORCE MICROSCOPY (AFM)

This section provides the surface profile measured from atomic force microscopy (AFM). The AFM topography is shown in Fig. SV. The AFM crosscut perpendicular to the fiber alignment direction (dashed line in Fig. SV(A)) is shown in Fig. SV(B). Calculated RMS roughness is ~ 70 nm, and the maximum peak-to-valley difference is ~ 360 nm. The height difference indicates the surface inhomogeneity over length scales comparable to the optical wavelength (515 nm) used, explaining the intense optical scattering observed in the TG experiment.

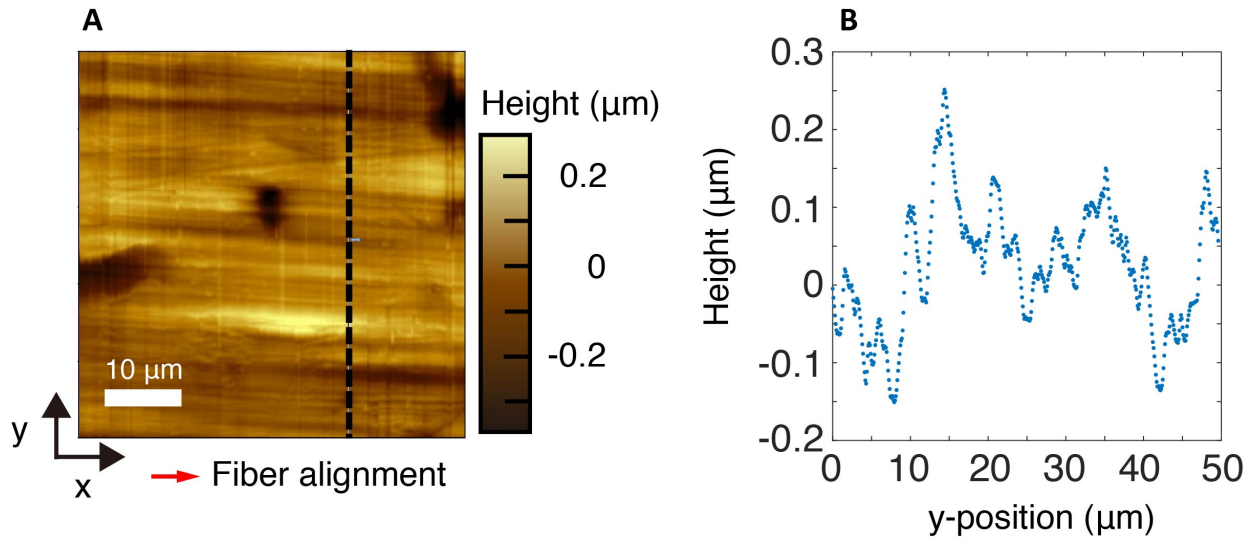


Figure SV. AFM Characterization of the UHMWPE surface. A. AFM topographic image of the sample. The x- and y- direction indicates parallel (perpendicular) to the fiber alignment. B. AFM crosscut along the dashed line in (A). RMS roughness is calculated to be ~ 70 nm, and the maximum peak-to-valley difference is ~ 360 nm.

-
- [1] Hiroyuki Fujishiro, Manabu Ikebe, Tomoyuki Naito, Koshichi Noto, Shuichi Kohayashi, and Shuji Yoshizawa. Anisotropic thermal diffusivity and conductivity of YBCO(123) and YBCO(211) mixed crystals. i. *Japanese Journal of Applied Physics*, 33(Part 1, No. 9A):4965–4970, sep 1994. doi: 10.1143/jjap.33.4965. URL <https://doi.org/10.1143/jjap.33.4965>.
- [2] S Burgess and D Greig. The low-temperature thermal conductivity of two-phase amorphous polymers. *Journal of Physics D: Applied Physics*, 7(15):2051–2057, oct 1974. doi:10.1088/0022-3727/7/15/309. URL <https://doi.org/10.1088/0022-3727/7/15/309>.
- [3] Yanfei Xu, Daniel Kraemer, Bai Song, Zhang Jiang, Jiawei Zhou, James Loomis, Jianjian Wang, Mingda Li, Hadi Ghasemi, Xiaopeng Huang, Xiaobo Li, and Gang Chen. Nanostructured polymer films with metal-like thermal conductivity. *Nature Communications*, 10(1):1–8, April 2019. ISSN 2041-1723. doi: 10.1038/s41467-019-09697-7. URL <https://www.nature.com/articles/s41467-019-09697-7>.